

Article

Development and Research Application of Optical Waveguide Microstructure Component Manufacturing Process for Triangle Roller Imprinting

Yung-Jin Weng *, Min-Ko Tsai and Jian-Zhi Chen

Department of Mechanical and Energy Engineering, National Chiayi University, Chiayi 60004, Taiwan

* Correspondence: yjweng@mail.ncyu.edu.tw

Abstract: This research integrates the stable pressuring of the flat surface of roll-to-plate (R2P) imprinting, the fast production features of roll-to-roll (R2R) imprinting, and compound layer ring-type microstructure mold cavity manufacturing technology. Using the compound multilayer method with air molecule assistance, the stability of the roller imprinting process is enhanced. In addition, with precision modulation of the triangle roll-to-plate (TR2P) system, a stable microstructure roller imprinting manufacturing process is achieved. The experimental results indicate that the developed triangle roll-to-plate system can stabilize the imprinting process of the continuous microstructure array components. Also, by modulating the angles of the roller axis and the ring, the exterior features of the microstructure can also be adjusted. Gas-molecule-assisted continuous pressuring effectively elevated the roll imprinting angle and continuous pressuring time and reached a high replication rate of 99.14%. The optical waveguide microstructure component produced by this process and the average waveguide propagation losses of approximately 1.2~1.4 dB/cm show that it has optical stability and transparency after optical testing. The research proves that the manufacturing process can effectively provide an innovative process for the equipment and application of the microstructure component.



Citation: Weng, Y.-J.; Tsai, M.-K.; Chen, J.-Z. Development and Research Application of Optical Waveguide Microstructure Component Manufacturing Process for Triangle Roller Imprinting. *Processes* **2023**, *11*, 2888. <https://doi.org/10.3390/pr11102888>

Academic Editor: Raul D. S. G. Campilho

Received: 15 September 2023
Revised: 26 September 2023
Accepted: 27 September 2023
Published: 30 September 2023



Copyright: © 2023 by the authors. Licensee MDPI, Basel, Switzerland. This article is an open access article distributed under the terms and conditions of the Creative Commons Attribution (CC BY) license (<https://creativecommons.org/licenses/by/4.0/>).

Keywords: triangle roller; roll imprinting; microstructure; microsystem; waveguide

1. Introduction

With the rapid advancement of science and technology, developing compact and lightweight wearable consumer electronic products and high-speed micro-components has become one of the main directions for research and development. The technology of the microsystem component manufacturing process is usually used in advanced scientific technology industries such as microsystems, opto-mechatronics, biomedicine, display monitors, opto-electrics, optics, and information communication. Microsystem components are usually used as the key to enhancing product efficacy and bringing scientific products into reality, for example, in the array grating, phased-array lens, diffusion membrane, and light guide plate of the backlighting modules of LCD monitors; the microchannel structure used for examining diabetes or cancers in biomedical engineering [1–3]; and the micro-lens structure [4–12] for capturing images in the 3C industry. Optical waveguide components have been applied in microsystems to transmit optical signals. Arrayed waveguide grating is a primary research focus that has been applied in the passive components of consumer electronics. Currently, waveguides are produced using semiconductor processes such as chemical vapor deposition (CVD) and reactive ion etching (RIE). In addition, the intermediate core layer, with a high refractive index, and the external cladding layer, with a low refractive index, must be considered in the production of optical waveguide components so that the light can be stabilized when transmitting optical signals within the core layer. The technology of the manufacturing process for micro-nano imprinting, in terms of forming technology, can be classified into the following three types: plate-to-plate [13,14],

roll-to-plate [15–19], and roll-to-roll [20–30]. Each type has its own appropriate situation for application and advantages and, of course, disadvantages. The advantages are described above. As for disadvantages, one example is uneven pressure during imprinting in the P2P type. Also, the speed is limited for the R2P and R2R types because retardant flow filling during the process of roll imprinting forming is affected by the viscosity, level of microstructure, roll imprinting temperature, and degree of forming force, which results in a minimum required time for filling in order to complete the entire roll imprinting duplication. Thus, it is impossible to achieve the demand for immediate adjustment and fast mass production. This research focuses on the development and application of an optical waveguide microstructure component manufacturing process for triangle roll-to-plate imprinting. In the process of continuous roller printing mass production, the system controlling the pressure stability of the roller printing process is important because the microstructure components are affected by rebound and elastic recovery factors in the forming process. Therefore, before forming is completed, the single roller structure must roll at a very slow speed to ensure the high replicative formability of the microstructure feature size, but this will fail to meet the requirements for mass production. However, if belt-type surface contact roller printing is used, the continuous pressure retention of the middle area of the rolling belt is not considered, so the pressure must be ensured before forming. The present roller printing forming system cannot yet effectively overcome this problem; therefore, it is an urgent problem in current academic research. This study aims to use optical waveguide components as the microstructure components for the development and testing of the proposed system and to utilize the innovatively developed process technology for the roller printing of arrayed optical waveguide components. The self-installed light loss detection system is applied to detect the light loss, so as to check the stability of the novel manufacturing process of the triangle roller imprinting system. All of the above are problems that need to be addressed and explored.

In summation, this research undertakes the exploration of innovative design development and application using the compound multilayer method with air molecule assistance to enhance the stability of the roller imprinting process. In addition, by improving the precision modulation of the triangle roll-to-plate (TR2P) system, a stable microstructure roller imprinting manufacturing process is achieved. Improving the manufacturing process of microstructure triangle R2P imprinting can provide another effective innovative technology in the manufacturing process for microsystem and microstructure components with relevant results.

2. Materials and Methods

2.1. Basis for Equipment Design for Triangle Roller Manufacturing Process

To prevent the equipment from deformation during the down-pressing process in the research, a design for the minimal roller diameter is necessary. Because the research was conducted using a continuous manufacturing process of a micro-nano microstructure, it was necessary to undertake even more precise design evaluations before manufacturing a roll imprinting system in order to prevent deformation or damage to the roller from too great of a shearing force, which would produce discrepancies or inaccuracies during the imprinting process. By employing the distortion energy theory as a basis for the shearing force design of endurance strength, the shearing force on the triangle roller during down pressing could be determined.

2.1.1. Distortion Energy Theory to Estimate Roller Design

In this part, the main discussion is on gas assistance to propel the pneumatic cylinders to produce a thrust that pushes the roller at both ends as the down force of the roll imprinting process. The ends of the roller contain bearings, so the down force will not interfere with the turning of the roller, as illustrated in Figure 1.

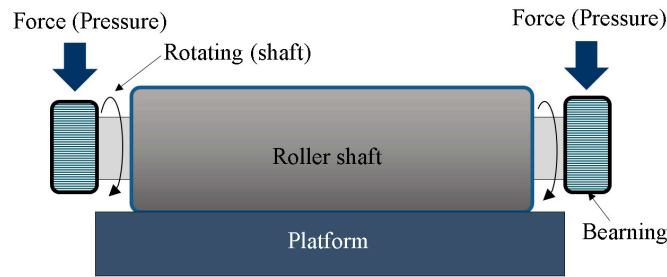


Figure 1. Gas-assisted propelling of pneumatic cylinder drive rod to work on both ends of the roller to actuate triangular roll-to-plate (TR2P) imprinting.

There is a shearing force produced while applying a down force. Roll imprinting that applies force on both ends of the roller produces a shearing force. According to the design principle of material mechanics, the maximum shear at the roller (τ_{max}) can be expressed as:

$$\tau_{max} = 4V/3A$$

where V : vertical shear force and A : area of the cross-section of the roller.

At the same time, taking into account the stress concentration (K), our research used a ball bearing with a sharp fillet. In terms of stress concentration, this research set $K = 2.5$; thus, the maximum shear of the roller can be revised to:

$$\tau_{max} = K(4V)/3A$$

This research uses the distortion energy theory as a basis for the design of endurance strength. According to the von Mises–Hencky theorem, because the design of the roller uses a ductile material (aluminum), the basis of the design for the safety range is within the following disruptive standard line formula (Figure 2):

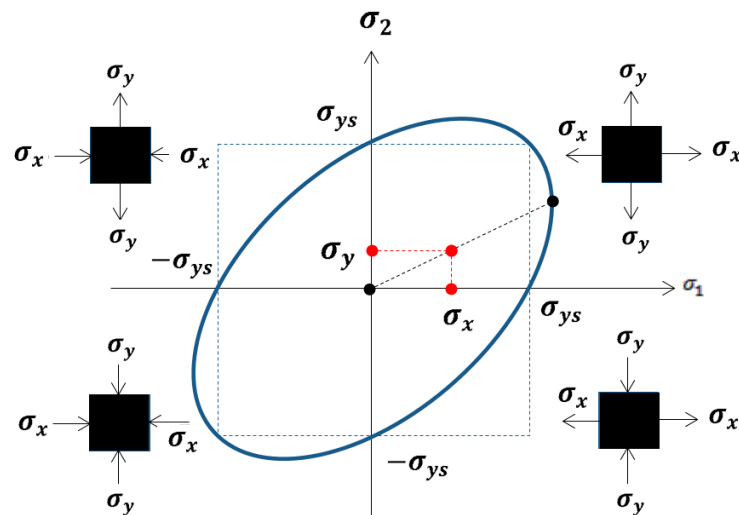


Figure 2. Distortion energy theory disruptive standard line.

$$(\sigma_x - \sigma_y)^2 + (\sigma_y - \sigma_z)^2 + (\sigma_z - \sigma_x)^2 < 2\sigma_{ys}^2$$

In terms of plane stress ($\sigma_z = 0$), the disruptive standard line formula of the distortion energy theory is as follows:

$$(\sigma_1)^2 - \sigma_1\sigma_2 + (\sigma_2)^2 = \sigma_{ys}^2$$

The resistance to the loading of the safety factor (*SF*) ratio,

$$\sigma_1/\sigma_2 = \sigma_x/\sigma_y \text{ is then}$$

$$\sigma_1 = \sigma_x\sigma_y / \sqrt{\sigma_x^2 - \sigma_x\sigma_y + \sigma_y^2}$$

$$SF = \sigma_1/\sigma_x = \sigma_y / \sqrt{\sigma_x^2 - \sigma_x\sigma_y + \sigma_y^2}$$

A steady torque is defined as $\sigma_x = -\sigma_y$, $\sigma_z = 0$, and $\tau_y = \sigma_x$.

$$\tau_{design} = \sigma_y / \sqrt{3} \tau_{max} = 0.557\sigma_{ys}$$

σ_{ys}' denotes that σ_{ys} has taken into account other situations of endurance:

$$SF = 0.557\sigma_{ys}' / \tau_{max}$$

$$K(4V)/3A = 0.557\sigma_{ys}'/N, \text{ setting } K = 2.5$$

$$SF = 0.1732\sigma_{ys}'(A)/V$$

Because the cross-sectional area of the roller is $A = \pi D^2/4$, the designed roller is as illustrated in Formula (1):

$$D = (7.35(V)(SF)/\sigma_{ys}')^{1/2} \quad (1)$$

where D is the diameter of the roller shaft.

2.1.2. Constructing an Adjustable Thermal Cavity Tensile Test System to Precisely Calculate the Minimum Roller Diameter to Prevent Micro-Distortion

The interference with precision due to the number of operations and the increased roller temperature during the manufacturing process in actual operation must be reflected. For this part of the research, we constructed an adjustable thermal cavity tensile test system (Figure 3) to conduct tensile testing to derive the yield stress range of the roller material to meet safety standards.

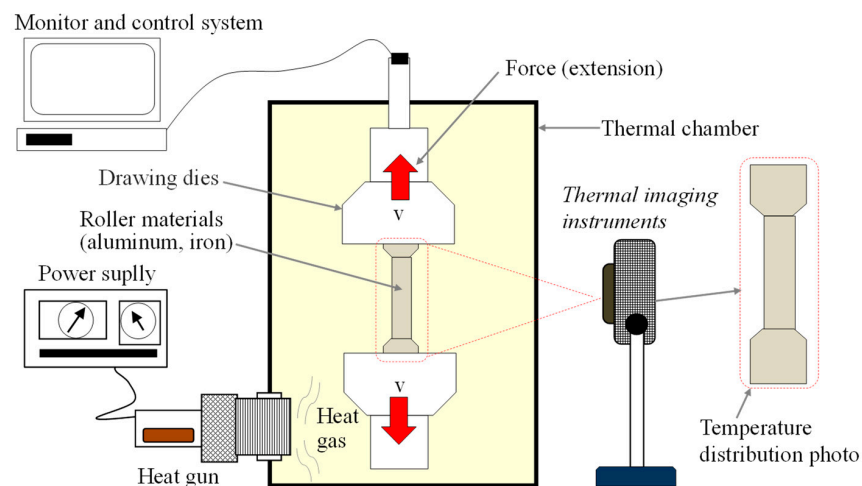


Figure 3. Adjustable thermal cavity tensile testing system schematic diagram.

The research initially employed tensile experimental testing under non-isothermal experimental parameters of 30, 40, 50, and 60 degrees on an aluminum roller material. The results showed that the maximum yield stress for aluminum was $\sigma_{ys} = 137$ MPa, and the

minimum yield stress within the above temperature range was $\sigma_{ys} = 110$ MPa. At the same time, this research set the safety factor (SF) at 3 and the estimated air pressure at no greater than 10 N. Inserting these settings into the formula above, the D values become 1.269 mm and 1.415 mm. Therefore, in order to prevent micro-distortion on the roller, the diameter of the designed roller must be greater than 1.415 mm.

2.2. Gas-Assisted Continuous Pressure Theory and Design Plan

2.2.1. Gas-Assisted Continuous Pressure Theory

In order to reduce rebounding and make roll imprinting more precise, this research adopted gas molecule-assisted continuous pressuring based on the gas kinetic formula and assumed the unit mass of gas (m) and its velocity (V_1) collided with the belt at high speeds (relative unit area), creating continuous contact between the belt and roll imprinting belt.

When

$$\begin{aligned} t = t_1, \text{ then } V &= V_1 \\ t = t_2, \text{ then } V &= V_2 \end{aligned}$$

The initial momentum of a single gas molecule plus the increased/decreased impulse momentum during the time interval from t_1 to t_2 (where t_1 is the starting time of the gas molecule touching the belt and t_2 is the ending time with the belt) equals the end momentum, as Formula (2) demonstrates:

$$\begin{aligned} \sum \int_{t_1}^{t_2} \vec{F} dt &= \int_{V_1}^{V_2} dV = mV_2 - mV_1 \\ m\vec{v}_1 + \sum \int_{t_1}^{t_2} \vec{F} dt &= m\vec{v}_2 \end{aligned} \quad (2)$$

If this is based on x , y , and z coordinate vectors, the following three pure scalar formulas are derived:

$$\begin{aligned} m_{gas}(V_x)_{start} + \sum \int_{t_{start}}^{t_{end}} F_x dt &= m_{gas}(V_x)_{end} \\ m_{gas}(V_y)_{start} + \sum \int_{t_{start}}^{t_{end}} F_y dt &= m_{gas}(V_y)_{end} \\ m_{gas}(V_z)_{start} + \sum \int_{t_{start}}^{t_{end}} F_z dt &= m_{gas}(V_z)_{end} \end{aligned}$$

If G is the center of mass of the gas (down pressure), then

because $m_{all-gas} = \sum m_{gas}$

$$m_{gas} \vec{r}_G = \sum m_{gas}$$

After differentiating, Formulas (3) and (4) are derived:

$$m_{gas} \vec{V}_G = \sum m_{gas} \vec{V}_i \quad (3)$$

$$m_{gas}(V_G)_{start} + \sum \int_{t_{start}}^{t_{end}} \vec{F}_i dt = M(V_G)_{end} \quad (4)$$

Assuming

m : mass of a single molecule;

m' : mass of the relative area of the belt that the gas molecule is colliding with; and

$$m'' = m + m'$$

then

$$mV_1 + m'V' = m''V''$$

In addition, our study takes asymmetrical roll imprinting into consideration because the system can control the velocity of the gas (V). Therefore, with the concept of moment of momentum as the principle of the asymmetrical forming of the system, the value of the torque and the angle of the slanted roll imprinting can be derived. The moment of momentum (H_o) is illustrated in Formula (5):

$$(H_o)_z = (d)(mV)$$

$$H_o = \vec{r} \times m\vec{V} = \begin{vmatrix} \vec{i} & \vec{j} & \vec{k} \\ r_x & r_y & r_z \\ mV_x & mV_y & mV_z \end{vmatrix} \quad (5)$$

The torque at point O (\vec{M}_o) from the force of the gas can be deduced (assuming the mass of the gas molecule remains constant) as shown in Formula (6):

$$\begin{aligned} \sum \vec{F} &= m\vec{V}; \\ \sum \vec{M}_o &= \vec{r} \times \sum \vec{F} = \vec{r} \times m\vec{V} \\ \dot{H}_o &= \frac{d}{dt}(\vec{r} \times m\vec{V}) = \dot{\vec{r}} \times m\vec{V} + \vec{r} \times m\dot{\vec{V}} \\ \dot{\vec{r}} \times m\vec{V} &= m(\dot{\vec{r}} \times \vec{r}) = 0 \\ \text{then, } \sum \vec{M}_o &= \dot{H}_o \end{aligned} \quad (6)$$

The above formula also explains the rate of change in angular momentum versus time at point O, which is also the torque that leads to asymmetrical imprinting.

2.2.2. Analysis of Gas Molecule Pressuring System and Design Selection

This part of the research adopted analysis software to undergo simulation design analysis of the gas molecule pressuring system for the gas pressure and gas flow. As the basis of the design selection, the flow rate of the stabilized pressure for the simulation was set at 26–27 m/s. This research designed gas molecule pressuring array-type and radial-type systems for gas outlet distribution (specifications: 130 mm × 100 mm × 10 mm, thickness: 3 mm), as illustrated in Figure 4.

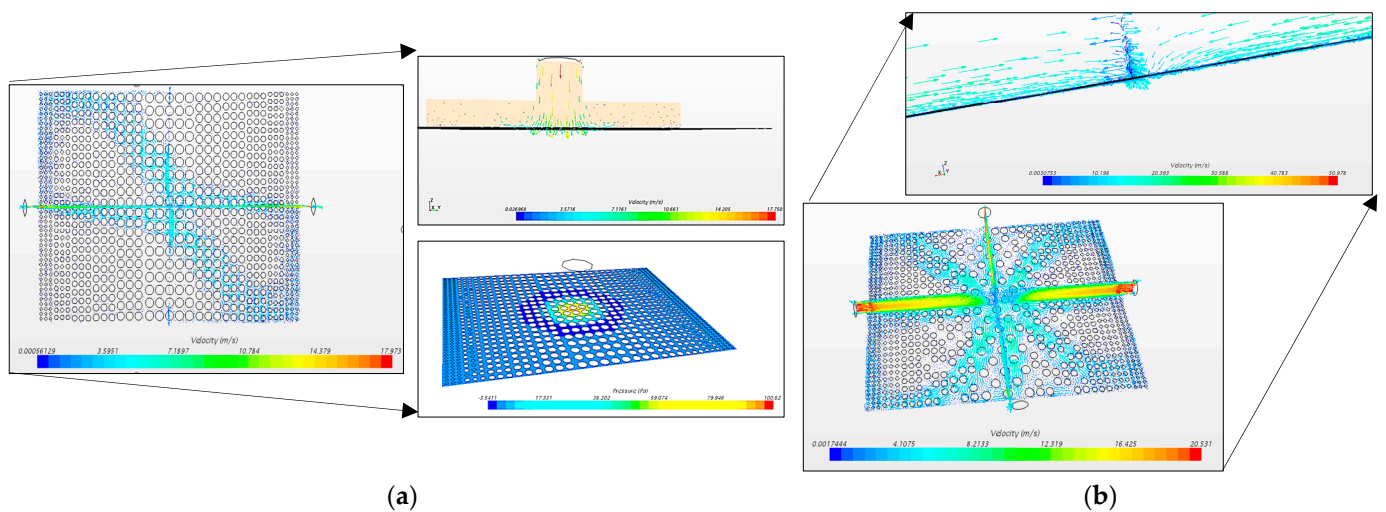


Figure 4. Gas molecule pressuring system: (a) array-type and (b) radial-type.

The diameter for the air inlets was 7 mm, and the diameters for the air outlets were 1 mm and 2 mm, to be distributed evenly at the bottom. The results of the simulations showed that the radial-type system had a better pressure distribution of gas molecules (Figure 5) and was thus used as the pressuring system.

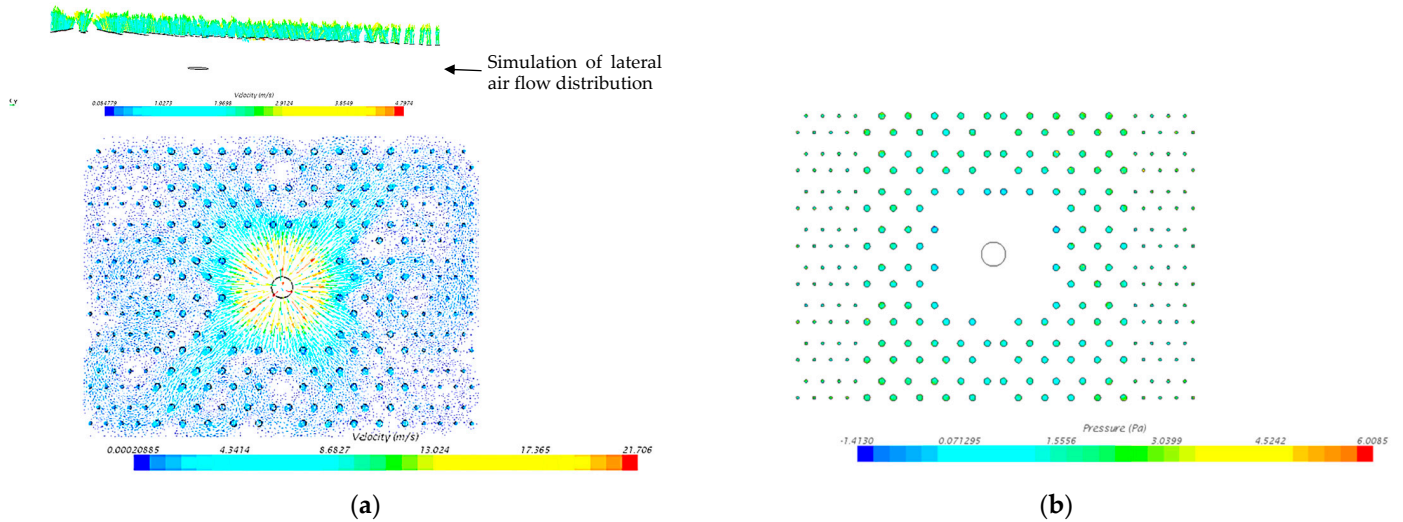


Figure 5. Radial-type gas molecule pressuring system: (a) air stream distribution schematic diagram and (b) air pressure distribution schematic diagram.

2.3. Equipment Development and Construction of the Manufacturing Process: Construction and Material Selection for the Microstructure Mold

The manufacturing process equipment developed in this research (Figure 6) was designed to have stable imprinting pressure. Figure 7 presents the results of the imprinting uniformity testing and the testing of the soft plate in non-structural ring belt imprinting and gas pressuring in the middle area.

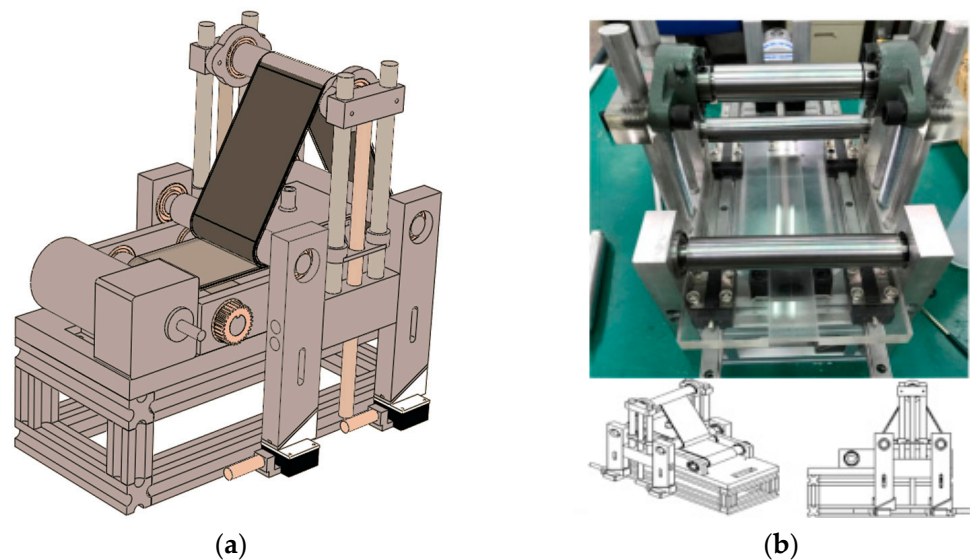


Figure 6. Manufacturing process equipment: (a) system schematic diagram and (b) actual schematic diagram (without ring belt), 3-D schematic diagram, and side view.

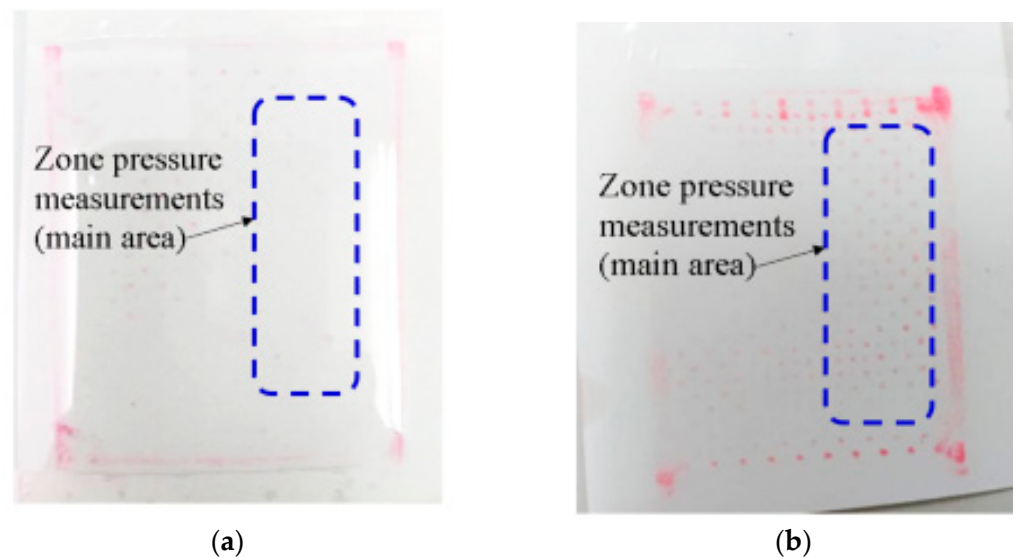


Figure 7. Middle area of ring belt in imprinting uniformity testing: (a) no pressure and (b) testing result of gas molecule-pressured soft plate.

A micro-electric manufacturing process was used to produce a middle-beam microstructure array (this is not discussed here due to its commonality) with multilayer casting to create a compound layer ring belt microstructure mold. The compound ring belt will prevent distortion of the microstructure from tensile stress and shear during the roll imprinting process. The ring belt microstructure mold was then installed on the triangle roller. In addition, the exposure curing system had edge lighting as the direction of light.

2.4. Exploration Examining the Mechanical Properties of the Compound Ring Belt Microstructure Mold

In this part of the research, we made a compound ring belt from PDMS compound carbon fiber layers and derived the average maximum tensile strength of 1157.22 MPa after tensile testing (Table 1) to prevent stretching distortion from too great a driving force during triangle roller imprinting. Moreover, after nano-indentation testing, the pure PDMS (10:1) elastic modulus was 1.85 MPa. In addition, the average indentation elastic modulus of the carbon fiber compound ring belt due to the base effect of the carbon fiber was increased to 5.016 MPa after nano-indentation testing (Table 2).

Table 1. PDMS (10:1) compound carbon fiber ring belt.

Test (Times)	Young's Modulus (MPa)
1	1123.36
2	1102.34
3	1202.31
4	1104.56
5	1187.38
6	1202.39
7	1178.15
Average	1157.21

Table 2. Compound carbon fiber ring belt nanoindentation testing.

Test (Times)		Nanoindentation Elastic Modulus (MPa)	
1		4.82	
2		4.58	
3		5.04	
4		5.31	
5		5.33	
Average		5.016	

Temperature (°C)	Test (Times)	Nanoindentation elastic modulus (MPa)	
		Data	Average
30	1	4.89	4.91
	2	4.93	
40	1	4.95	4.985
	2	5.02	
50	1	5.01	5.07
	2	5.13	
60	1	4.95	5.08
	2	5.21	
70	1	5.23	5.33
	2	5.43	

After testing at different temperatures (30 °C, 40 °C, 50 °C, 60 °C, and 70 °C), all were higher than the pure PDMS elastic modulus; thus, providing strength to the mold's microstructure would help to maintain the integrity of the microstructure during the roll imprinting process.

2.5. Procedure and Mechanism of Triangle Roller Imprinting and Reversal Imprinting Processes

The procedure of roll imprinting in our research was conducted in the following order: (a) Install a microstructure ring belt adjusted to proper tightness. (b) Place a photoresist agent on the substrate. (c) Adjust the pressure needed, the angles of the microstructure ring belt, and the relative parallel and non-parallel angles between the substrates. Start triangle roller imprinting and turn on the UV light for curing at the same time. (d) Turn off the UV light and remove the mold to produce a microstructure product. The difference between the reversal imprinting process and roll imprinting is seen at Step (b), where the photoresist agent was provided to the belt microstructure by a fill-scraping system to undergo the imprinting transfer. Steps (c) and (d) are the same. At the end, conduct reactive-ion etching (RIE) to remove the residual photoresist agent and arrive at the product, as illustrated in Figure 8.

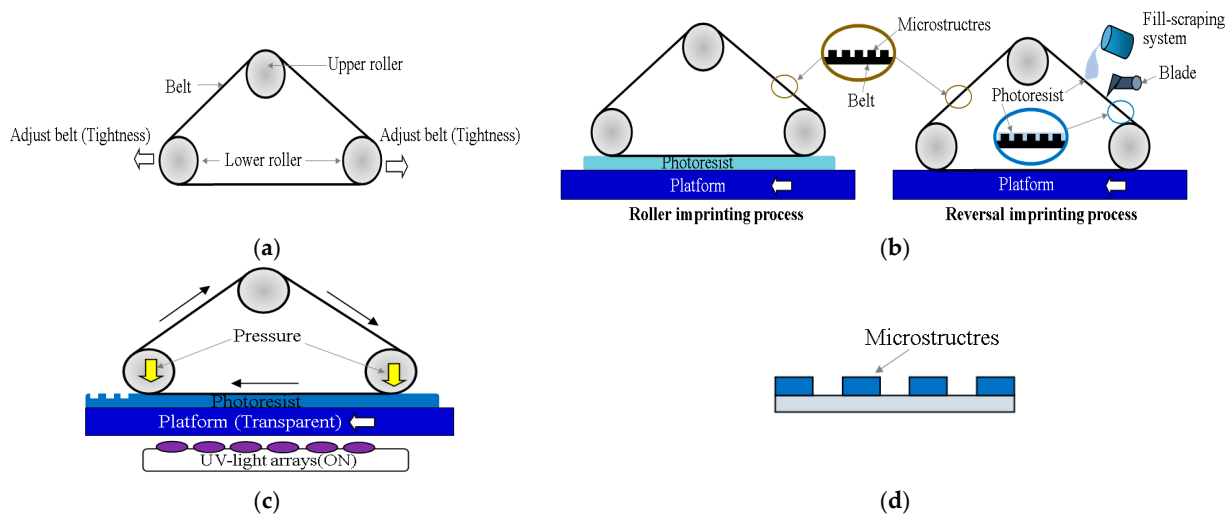


Figure 8. The procedure of roll imprinting: (a) Install a microstructure ring belt adjusted to the proper tightness. (b) Place a photoresist agent on the substrate (roll imprinting and reversal imprinting process). (c) Adjust the pressure needed, and the angles of the microstructure ring belt, and the relative parallel. Start triangle roller imprinting, and turn on UV light for curing at the same time. (d) Turn off the UV light and remove the mold to produce a microstructure product.

3. Results and Discussion

3.1. Analytical Exploration of the Distribution of Ring Belt Pressure

In this part, the ring belt stress and stress distribution simulation (equivalent stress and vector principal stress) were undertaken by setting a 10:1 ratio of the main agent to a hardener in the PDMS (PDMS simulation parameters: density: 965 kg/m³; Young’s modulus: 1.72 MPa; Poisson’s ratio: 0.495) using an aluminum roller (aluminum simulation parameters: density: 2775 kg/m³; Young’s modulus: 71,100 MPa; Poisson’s ratio: 0.325) with a diameter of 30 mm and length of 150 mm. Figure 9 shows the results of the experiment with three groups of simulations using a PDMS thickness of 5 mm. For the Group A simulation, the right roller pressure was set at 0.02 MPa. For the Group B simulation, the left and right roller pressures were set at 0.02 MPa. For the Group C simulation, the left and right roller pressures were set at 0.02 MPa, and the middle area under pressure was set at 0.02 MPa.

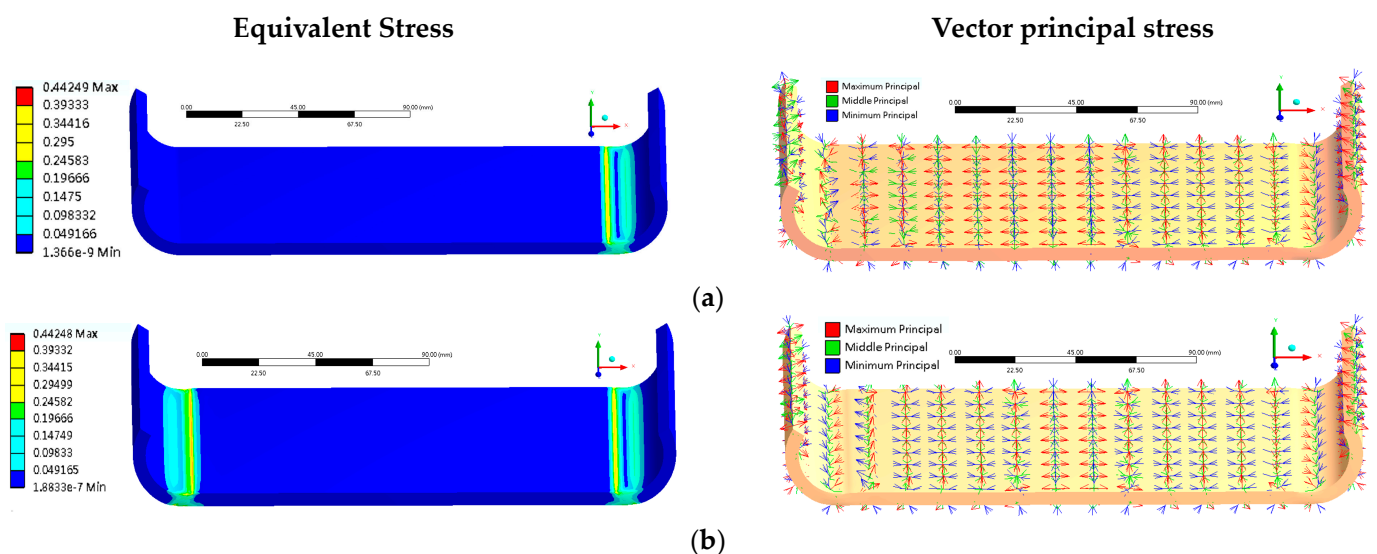


Figure 9. Cont.

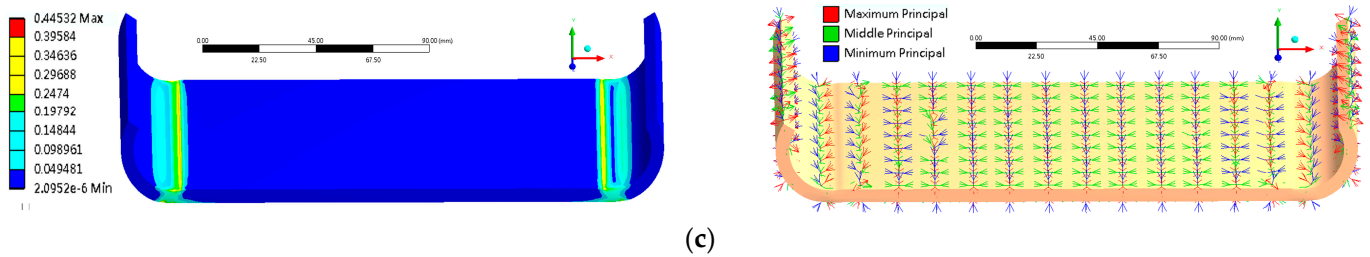


Figure 9. Stress of ring belt roll imprinting and simulation of stress distribution: (a) the right roller pressure was set at 0.02 MPa; (b) the left and right roller pressures were set at 0.02 MPa; and (c) the left and right roller pressures were set at 0.02 MPa, and the middle area under pressure was set at 0.02 MPa.

After analysis, the pressure distribution was more even and stable in the Group C simulation and performed better in terms of distortion after roll imprinting than those of the Group A and Group B simulations.

3.2. The Inference of Triangle Roller Imprinting Mode on Forming Rate of Roll Imprinting

In this part of the research, three modes were employed. Model A: single-side roller pressuring, Model B: double-side roller pressuring, and Model C: double-side roller pressuring combined with uniform gas pressuring in the middle area of the ring belt (Figure 10). Table 3 and Figure 11 infer the replication forming rates of the three roll imprinting modes under the same experimental parameters.

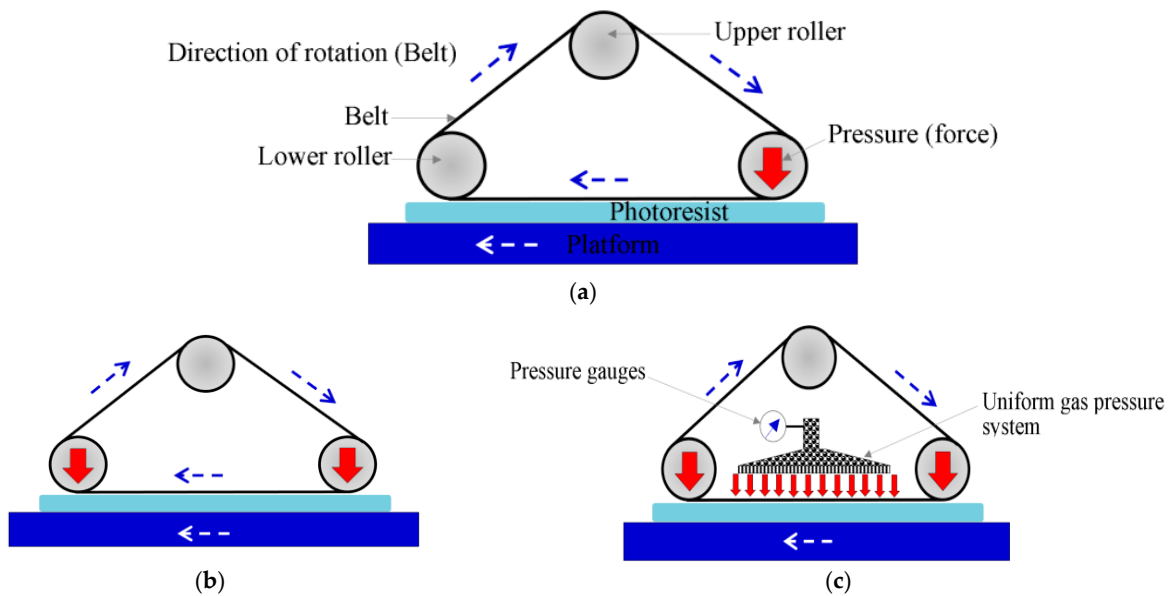


Figure 10. Side view of triangle roller imprinting modes schematic diagram: (a) Model A, (b) Model B, and (c) Model C.

Table 3. Inference of replication forming rate by three types of roll imprinting modes.

Model	Replication Forming Rate					Average (Replication Forming Rate)
	Test (Times)					
	1	2	3	4	5	
A	96.8%	95.3%	96.2%	94.7%	95.3%	95.66%
B	97.0%	95.7%	96.2%	97.4%	95.8%	96.42%
C	98.5%	99.3%	99.1%	99.5%	99.3%	99.14%

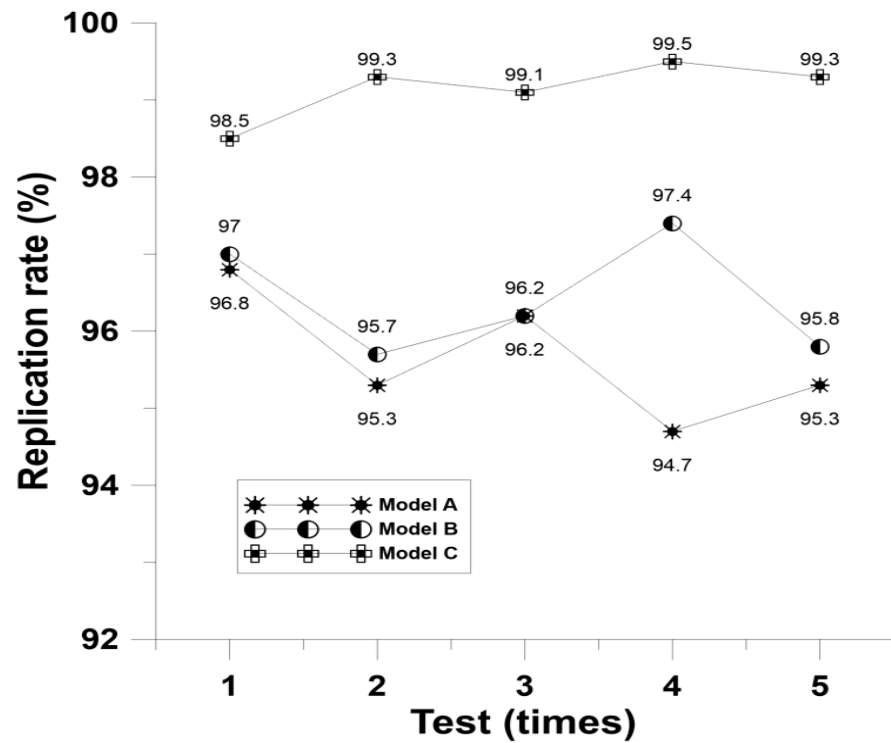


Figure 11. Inference of replication forming rates by three types of roll imprinting modes under the same roll imprinting experimental parameters.

The results of the experiment showed that the forming rate and replication rate of the microstructure in Model C were the highest, Model B the second highest, and Model A the lowest. The forming rates were different because the range between the entering imprinting angle and exiting imprinting angle can be viewed as the total forming angle in the roll imprinting process. In Model C, after the roller exited out of the total angle, there was still continuous forming pressure on the middle area of the ring belt providing the force needed to stop the rebounding of the formed microstructure, indirectly elevating the exiting angle and increasing the total angle. Therefore, there was more forming time under the fixed rpm. From Table 3, the replication rates of Model C were 3.48% and 2.72% higher than those of Model A and Model B, respectively. The replication rates of Model A and Model B were closer to each other, with only a 0.76% difference. Although Model C can achieve a replication rate as high as 99.14%, it still needs 0.76% to reach a 100% complete replication rate. One reason might be, in the opinion of the researchers, that the roll imprinting forming and UV curing time (position) occurred too early in that part of the process. Thus, the photoresist agent absorbed the UV light before roll imprinting forming, resulting in premature cross-link curing of the molecular bonding. Furthermore, when the maximum gas-molecule-assisted force is no greater than the roller force in the middle area of the ring belt, it will help elevate the microstructure replication rate as the gas-assisted uniform force is increased.

3.3. The Inference of Triangle Roller Imprinting on the Roll Imprinting Forming of the Ring Belt and Substrate with an in-between Angle

This part of the research mainly explores Models A, B, and C of the above section to achieve a large area of grayscale array of micro-junctions by providing an angle between the ring belt microstructure array and the tilting of the substrate for roll imprinting forming. The imprinting transfer angle is derived by examining the product, checking the depth h_n of the roll imprinting, and measuring the length L_n of the area of distribution of the microstructure. Through triangulation calculations, the tilting angle after roll imprinting can be derived using Formula (7) (Figure 12).

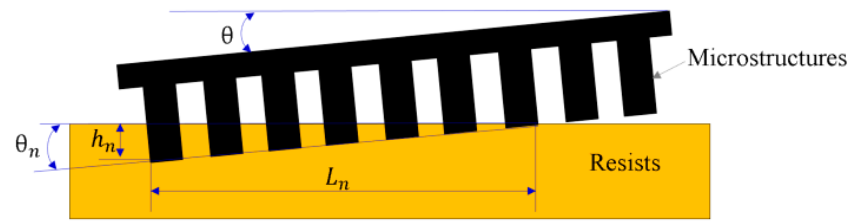


Figure 12. Inclined angle measuring method before and after roll imprinting.

The results of the experiment were that the average replication rate of Model A was 80.638%, of Model B was 85.56%, and of Model C was 96.428%, as illustrated in Table 4.

Table 4. Inference of grayscale replication forming rate by three types of roll imprinting mode.

Model	Replication Forming Rate					Average (Replication Forming Rate)
	Test (Times)					
	1	2	3	4	5	
A	78.82%	80.83%	83.21%	80.45%	79.88%	80.638%
B	83.73%	85.75%	87.44%	83.53%	85.35%	85.56%
C	94.73%	97.37%	96.32%	96.75%	96.97%	96.428%

The results indicate that Model C still had the best forming rate in terms of grayscale angle (inclined angle, θ_n). The replication rate of the angled roll imprinting process is given by:

$$\theta_n = \tan^{-1} \left(\frac{h_n}{L_n} \right) \quad (7)$$

where θ_n is the inclined angle of the microstructure mold.

3.4. Measurement of Optical Waveguide and Light Loss of Triangle Roller Imprinting

The feasibility of the optical waveguide component and light loss of the triangle roller imprinting was explored. Using a silicon wafer as the substrate, LPCVD sedimentation silicon dioxide as the buffer (power: 10 W; gas: $\text{SiH}_4/\text{N}_2\text{O}$; pressure: 0.6 torr; time: 300 min), and UV curable mr-L6000 polymer as the core layer material. Using Model C designed in this research, roll imprinting was executed. A PMMA material (molecular weight: 120 K; solvent: toluene; concentration: 14% wt) was used for the upper cladding to produce an optical waveguide component, as illustrated in Figure 13.

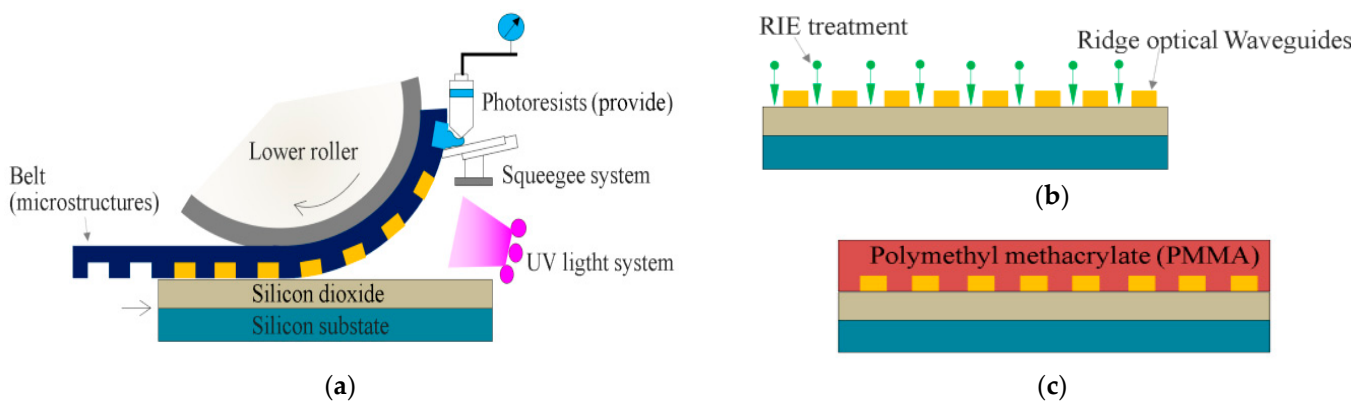


Figure 13. Optical waveguide component manufacturing process schematic diagram: (a) LPCVD sedimentation silicon dioxide buffer layer roll imprinting UV curable material, (b) reactive-ion etching to remove residual photoresist layer, and (c) upper cladding (PMMA).

Under the scale of the asymmetric mid-beam optical waveguide component of the experiment, light loss was measured using the researchers' own measurement system (Figure 14).

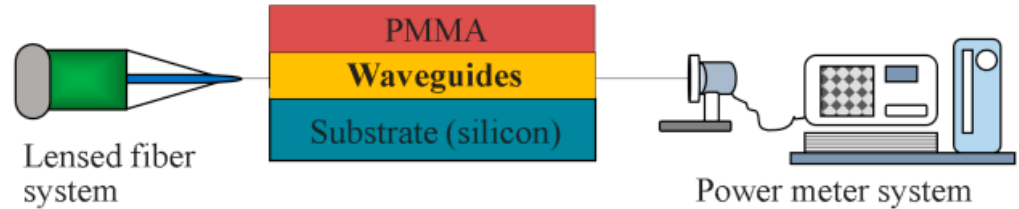


Figure 14. Schematic diagram of light loss measurement system.

Better light loss performance could be achieved using this manufacturing process as compared to that of a gas-assisted light-curing process. Light loss calculations are shown in Formula (8):

$$\text{Propagation loss of ridge optical waveguides (dB)} = 10 \log \left(\frac{P_{input}}{P_{output}} \right) \quad (8)$$

where

P_{input} : Power at the light propagation input end before entering the optical waveguide.

P_{output} : Power measured at the output end after the optical waveguide.

The average propagation loss of waveguides was approximately 1.2~1.4 dB/cm. There was less light loss and better light luminosity (Figure 15) because there were fewer defects inside the microstructure, resulting in a more complete imprinting transfer.

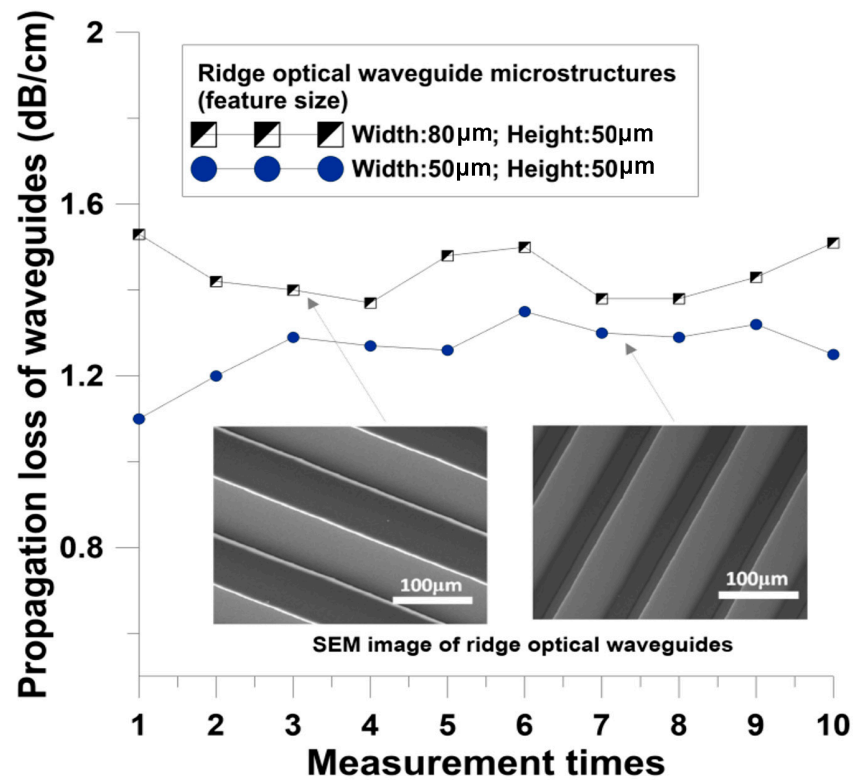


Figure 15. Diagram of propagation loss of waveguides.

4. Conclusions

This research focused on the development and application of a manufacturing process for triangle roller imprinting in which the distortion energy theory was used as the basis for designing the safety of the roller in terms of the endurance strength of the shearing force. In addition, an adjustable thermal cavity tensile testing system was constructed to calculate the minimum roller diameter that could prevent distortion and predict the exterior form of the microstructure formed from tilted roll imprinting of the triangle roller manufacturing process. In addition, a simulation analysis of gas-molecule-assisted continuous uniform pressing was conducted. At the same time, the research system's equipment was constructed. The carbon fiber compound layer ring belt microstructure maintained the structural integrity of the mold during the roll imprinting process, which was assisted by edge lighting to form the microstructure. The results of the experiment showed that among the three roll imprinting models, the gas-molecule-assisted continuous pressuring model effectively elevated the roll imprinting angle and continuous pressuring time and reached a high replication rate of 99.14%, while forming was achieved through optical waveguide component imprinting transfer. The average waveguide propagation loss was approximately 1.2~1.4 dB/cm, indicating that excellent light loss results were attained after examination.

Author Contributions: Conceptualization, Y.-J.W.; methodology, Y.-J.W., M.-K.T. and J.-Z.C.; software, Y.-J.W., M.-K.T. and J.-Z.C.; data curation, Y.-J.W., M.-K.T. and J.-Z.C.; writing—original draft preparation, Y.-J.W., M.-K.T. and J.-Z.C.; writing—review and editing, Y.-J.W.; funding acquisition, Y.-J.W. All authors have read and agreed to the published version of the manuscript.

Funding: This work was partially supported by the National Science and Technology Council (Series Nos. NSTC 111-2221-E-415-009 and NSTC 112-2221-E-415-014) of Taiwan, Republic of China.

Data Availability Statement: Not applicable.

Acknowledgments: The authors would like to thank all students who contributed to this study, the authors gratefully acknowledge the financial support provided for this study by the National Science and Technology Council of Taiwan, ROC.

Conflicts of Interest: The authors declare no conflict of interest.

References

1. Hitsumoto, T. Relationship between cardiovascular risk factors and hemorheology assessed by microchannel method in patients with type 2 diabetes mellitus. *Diabetol. Int.* **2017**, *8*, 316–322. [[CrossRef](#)] [[PubMed](#)]
2. Takeishi, N.; Ito, H.; Kaneko, M.; Wada, S. Deformation of a Red Blood Cell in a Narrow Rectangular Microchannel. *Micromachines* **2019**, *10*, 199. [[CrossRef](#)] [[PubMed](#)]
3. Kang, H.; Kim, J.; Cho, H.; Han, K.-H. Evaluation of Positive and Negative Methods for Isolation of Circulating Tumor Cells by Lateral Magnetophoresis. *Micromachines* **2019**, *10*, 386. [[CrossRef](#)] [[PubMed](#)]
4. Merlo, S.; Crisà, E.; Giusti, D.; Ferrera, M.; Soldo, M. Characterization of Tunable Micro-Lenses with a Versatile Optical Measuring System. *Sensors* **2018**, *18*, 4396. [[CrossRef](#)]
5. Yang, F.; Yan, W.; Tian, P.; Li, F.; Peng, F. Electro-Optical Imaging Technology Based on Microlens Array and Fiber Interferometer. *Appl. Sci.* **2019**, *9*, 1331. [[CrossRef](#)]
6. Xie, S.; Wan, X.; Yang, B.; Zhang, W.; Wei, X.; Zhuang, S. Design and Fabrication of Wafer-Level Microlens Array with Moth-Eye Antireflective Nanostructures. *Nanomaterials* **2019**, *9*, 747. [[CrossRef](#)]
7. Li, K.; Xu, G.; Huang, X.; Xie, Z.; Gong, F. Manufacturing of Micro-Lens Array Using Contactless Micro-Embossing with an EDM-Mold. *Appl. Sci.* **2019**, *9*, 85. [[CrossRef](#)]
8. Nagato, K.; Yajima, Y.; Nakao, M. Laser-Assisted Thermal Imprinting of Microlens Arrays—Effects of Pressing Pressure and Pattern Size. *Materials* **2019**, *12*, 675. [[CrossRef](#)]
9. Zhu, X.; Xu, Q.; Hu, Y.; Li, H.; Wang, F.; Peng, Z.; Lan, H. Flexible biconvex microlens array fabrication using combined inkjet-printing and imprint-lithography method. *Opt. Laser Technol.* **2019**, *115*, 118–124. [[CrossRef](#)]
10. Liu, Y.; Qiao, Z.; Qu, D.; Wu, Y.; Xue, J.; Li, D.; Wang, B. Experimental Investigation on Form Error for Slow Tool Servo Diamond Turning of Micro Lens Arrays on the Roller Mold. *Materials* **2018**, *11*, 1816. [[CrossRef](#)]
11. Liu, X.; Li, M.; Bian, J.; Du, J.; Li, B.; Fan, B. A Novel Fabricating Method of Micro Lens-on-Lens Arrays with Two Focal Lengths. *Micromachines* **2021**, *12*, 1372. [[CrossRef](#)] [[PubMed](#)]

12. Steblov, G.M.; Kogan, M.G.; King, R.W.; Scholz, C.H.; Bürgmann, R.; Frolov, D.I. Imprint of the North American plate in Siberia revealed by GPS. *Geophys. Res. Lett.* **2003**, *30*. [[CrossRef](#)]
13. Becker, H.; Heim, U. Hot embossing as a method for the fabrication of polymer high aspect ratio structures. *Sens. Actuators A Phys.* **2000**, *83*, 130–135. [[CrossRef](#)]
14. Ahn, S.H.; Guo, L.J. Large-Area Roll-to-Roll and Roll-to-Plate Nanoimprint Lithography: A Step toward High-Throughput Application of Continuous Nanoimprinting. *ACS Nano* **2009**, *3*, 2304–2310. [[CrossRef](#)]
15. Xu, Z.; Peng, L.; Lai, X. Investigation on the roll-to-plate microforming of riblet features with the consideration of grain size effect. *Int. J. Adv. Manuf. Technol.* **2020**, *109*, 2055–2064. [[CrossRef](#)]
16. Guembe, M.; Martín-Rabadán, P.; Cruces, R.; Granda, M.J.P.; Bouza, E. Roll-Plate Alone Does Not Demonstrate Colonization In Silicone Neonatal Catheters. *Pediatr. Infect. Dis. J.* **2016**, *35*, 351–353. [[CrossRef](#)]
17. Tahir, U.; Kamran, M.A.; Jeong, M.Y. Numerical Study on the Optimization of Roll-to-Roll Ultraviolet Imprint Lithography. *Coatings* **2019**, *9*, 573. [[CrossRef](#)]
18. Donie, Y.J.; Yuan, Y.; Allegro, I.; Schackmar, F.; Hossain, I.M.; Huber, R.; Roger, J.; Paetzold, U.W.; Gomard, G.; Lemmer, U. A Self-Assembly Method for Tunable and Scalable Nano-Stamps: A Versatile Approach for Imprinting Nanostructures. *Adv. Mater. Technol.* **2022**, *7*, 2101008. [[CrossRef](#)]
19. Kooy, N.; Mohamed, K.; Pin, L.T.; Guan, O.S. A review of roll-to-roll nanoimprint lithography. *Nanoscale Res. Lett.* **2014**, *9*, 1–3. [[CrossRef](#)]
20. Xu, J.; Liu, C.; Hsu, P.-C.; Liu, K.; Zhang, R.; Liu, Y.; Cui, Y. Roll-to-Roll Transfer of Electrospun Nanofiber Film for High-Efficiency Transparent Air Filter. *Nano Lett.* **2016**, *16*, 1270–1275. [[CrossRef](#)]
21. Arrif, T.; Benchabane, A.; Guermoui, M.; Gama, A.; Merarda, H. Optical performance study of different shapes of solar cavity receivers used in central receiver system plant. *Int. J. Ambient. Energy* **2018**, *42*, 81–95. [[CrossRef](#)]
22. Kim, J.; Hassinen, T.; Lee, W.H.; Ko, S. Fully solution-processed organic thin-film transistors by consecutive roll-to-roll gravure printing. *Org. Electron.* **2017**, *42*, 361–366. [[CrossRef](#)]
23. Tahir, U.; Kim, J.I.; Javeed, S.; Khaliq, A.; Kim, J.-H.; Kim, D.-I.; Jeong, M.Y. Process Optimization for Manufacturing Functional Nanosurfaces by Roll-to-Roll Nanoimprint Lithography. *Nanomaterials* **2022**, *12*, 480. [[CrossRef](#)] [[PubMed](#)]
24. Deng, B.; Hsu, P.C.; Chen, G.C.; Chandrashekar, B.N.; Liao, L.; Ayitimuda, Z.; Wu, J.X.; Guo, Y.F.; Lin, L.; Zhou, Y.; et al. Roll-to-Roll Encapsulation of Metal Nanowires between Graphene and Plastic Substrate for High-Performance Flexible Transparent Electrodes. *Nano Lett.* **2015**, *15*, 4206–4213. [[CrossRef](#)] [[PubMed](#)]
25. Lee, C.-Y.; Lee, S.-J.; Chen, C.-H.; Yang, L.-J.; Wang, X.-W.; Lin, J.-T.; Chao, P.-Y.; Chen, S.-Y. Application of Monitoring Module Three-in-One Microsensor to Real-Time Microscopic Monitoring of Polarizer Sheet in Roll-to-Roll Process. *Processes* **2022**, *10*, 900. [[CrossRef](#)]
26. Jo, M.; Noh, J.; Cho, G.; Lee, T.M.; Oh, B.; Nam, S.; Lee, C. Strain Optimization of Tensioned Web through Computational Fluid Dynamics in the Roll-to-Roll Drying Process. *Polymers* **2022**, *14*, 2515. [[CrossRef](#)]
27. Jo, M.; Lee, J.; Kim, S.; Cho, G.; Lee, T.-M.; Lee, C. Web Unevenness Due to Thermal Deformation in the Roll-to-Roll Manufacturing Process. *Appl. Sci.* **2020**, *10*, 8636. [[CrossRef](#)]
28. Krebs, F.C.; Gevorgyan, S.A.; Alstrup, J. A roll-to-roll process to flexible polymer solar cells: Model studies, manufacture and operational stability studies. *J. Mater. Chem.* **2009**, *19*, 5442–5451. [[CrossRef](#)]
29. Palavesam, N.; Marin, S.; Hemmetzberger, D.; Landesberger, C.; Bock, K.; Kutter, C. Roll-to-roll processing of film substrates for hybrid integrated flexible electronics. *Flex. Print. Electron.* **2018**, *3*, 014002. [[CrossRef](#)]
30. Park, H.J.; Kang, M.-G.; Ahn, S.H.; Guo, L.J. A Facile Route to Polymer Solar Cells with Optimum Morphology Readily Applicable to a Roll-to-Roll Process without Sacrificing High Device Performances. *Adv. Mater.* **2010**, *22*, E247–E253. [[CrossRef](#)]

Disclaimer/Publisher’s Note: The statements, opinions and data contained in all publications are solely those of the individual author(s) and contributor(s) and not of MDPI and/or the editor(s). MDPI and/or the editor(s) disclaim responsibility for any injury to people or property resulting from any ideas, methods, instructions or products referred to in the content.